JACS
JOURNAL OF THE AMERICAN CHEMICAL SOCIETY

Article

A Self-Assembled Organic/Metal Junction for Water Photo-Oxidation

Astrid J. Olaya, Terumasa Omatsu, Jonnathan C. Hidalgo-Acosta, Julieta S. Riva, Victor Costa Bassetto, Natalia Gasilova, and Hubert H. Girault

J. Am. Chem. Soc., **Just Accepted Manuscript** • DOI: 10.1021/jacs.9b02693 • Publication Date (Web): 09 Apr 2019

Just Accepted

ACS Publications

is published by the American Chemical Society. 1155 Sixteenth Street N.W., Washington, DC 20036

A Self-Assembled Organic/Metal Junction for Water Photo-Oxidation

Astrid J. Olaya[a]*, Terumasa Omatsu[b], Jonnathan C. Hidalgo-Acosta[a], Julieta S. Riva[a,c], Victor Costa Bassetto[a], Natalia Gasilova[a,†] and Hubert H. Girault[a]

[a] Laboratory of Physical and Analytical Electrochemistry, EPFL Valais Wallis, École Polytechnique Fédérale de Lausanne, CH-1951 Sion, Switzerland.

[b] Faculty of Molecular Chemistry and Engineering, Kyoto Institute of Technology, Kyoto, Japan.

[c] Consejo Nacional de Investigaciones Científicas y Técnicas, CONICET. Facultad de Matemática, Astronomía, Física y Computación, Universidad Nacional de Córdoba. Medina Allende s/n. Ciudad Universitaria, X5000HUA, Córdoba, Argentina.

[†] Present address: Institute of Chemical Sciences and Engineering, ISIC-GE, EPFL Valais Wallis, École Polytechnique Fédérale de Lausanne, CH-1951 Sion, Switzerland

* Corresponding author: astrid. olaya@epfl.ch, Phone +41 21 693 3655

Abstract

We report the *in-situ* self-assembly of TTF, $TTF^{\bullet+}$ and BF_4^- or PF_6^- into p-type semiconductors on the surface of Pt microparticles dispersed in water/acetonitrile mixtures. The visible light photoactivation of these self-assemblies leads to water oxidation forming O_2 and H^+, with an efficiency of 100 % with respect to the initial concentration of $TTF^{\bullet+}$. $TTF^{\bullet+}$ is then completely reduced to TTF upon photo-reduction with water. The Pt microparticles act as floating microelectrodes whose Fermi level is imposed by the different redox species in solution; here predominantly TTF, $TTF^{\bullet+}$ and $HTTF^+$, which furthermore showed no signs of decomposition in solution.

Keywords: Water Oxidation, Self-assembly, Tetrathiafulvalene, Redox Electrocatalysis, Photocatalysis.

Introduction

Inspired by the design of the 'Z-scheme' in Nature, photocatalytic or photoelectrochemical water splitting, also referred to as artificial photosynthesis, remains an attractive alternative to convert solar energy into chemical energy. [1-9] If much progress has been made on the photo-reduction of protons to hydrogen, a major deadlock is still the photo-oxidation of water to oxygen under visible light irradiation.[5]

The literature on water oxidation in aqueous media is extensive. [10-18] A common strategy to photochemically evolve O_2 involves either the direct absorption of visible light by a semiconductor, or the coordination of a molecular photosensitizer to the surface of a wide band gap semiconductor, such as TiO_2. [3, 5, 9] After photo-excitation, holes and electrons then migrate to the surface of the semiconductor and take part in the water oxidation reaction. [5, 9] In order to avoid recombination and increase efficiency, the carriers should be separated as far (or as long) as possible on the surface of a photocatalyst, where four successive charge separation events are required to release O_2. [3, 5, 9] Combining efficient visible light absorption, stable charge separation, and fast water oxidation catalysis is yet extremely challenging.

Significant progress has been achieved in the field of sensitisation of semiconductors using a wide range of metal complexes, organic dyes and porphyrins. [9] Ruthenium–polypyridyl complexes are extensively studied photosensitizers for water-splitting photo-anodes, due to their suitable redox potentials, good electrochemical stability, high molar absorptivity, long-lived excited-state lifetimes and broad coverage in the visible region. In addition, replacement of the ancillary ligands has proven to enhance significantly their performance. [9] Porphyrins have also been used to study photoinduced electron transfer to catalytic electron mediators. The absorption spectra of porphyrins are usually much broader than that of the Ru complexes, extending towards the near-IR, with high molar extinction coefficients. [9] The self-assembly of porphyrins is a reliable approach for the immobilization of zinc porphyrins on TiO_2.[9] Metal-free organic sensitizers are also potential candidates to replace expensive Ru-based complexes, exhibiting very high molar extinction coefficients (in the order of 100'000 $M^{-1}\cdot cm^{-1}$). Such sensitizers usually incorporate a donor group and an acceptor group (D-A), the later often anchored to the surface of the semiconductor. [9] One disadvantage of porphyrins and organic sensitizers is their tendency to aggregate, resulting in lower efficiencies due to faster recombination. Such problem can be partially overcome by introducing co-adsorbates or, bulky substituents in the synthesis of porphyrins. [9]

Photocatalytic-based junctions have also been widely studied for efficient water oxidation in both, suspension and photoelectrochemical devices. [5] Among the most widely reported junction-based systems one can find: [5] $BiVO_4$-based junctions ($BiVO_4$-WO_3, [19-21] $BiVO_4$-SnO_2-WO_3, [20] Co-Pi-$BiVO_4$-WO_3, [22] $CuWO_4$, [23] $BiVO_4$-ZnO[24-25], $BiVO_4$-TiO_2[26]), α-Fe_2O_3-based junctions (Co-α-Fe_2O_3–NA (nano arrays)/$MgFe_2O_4$, [27] α-Fe_2O_3-WO_3, [28] , NiO/α-$Ni(OH)_2$–α-Fe_2O_3,[29-30] IrO_2 (NP)-α-Fe_2O_3[31] and α-Fe_2O_3/$ZnFe_2O_4$), [32], WO_3-based junctions (Al_2O_3-WO_3 [33] and PtO_x-WO_3[34]) and Ag_3PO_4-based junctions (AgX/Ag_3PO_4 (X=Cl, I, Br) core–shell particles, [35] and $Ag@Ag_3(PO4)_{1-x}/ZnO$[36]).

Metal−molecule interactions can also play a key role in multi-electron charge-transfer reactions such as oxygen reduction, hydrogen evolution and water oxidation.[37] The catalysis of electron-transfer reactions on electrically floating conductive particles induced by a redox couple or "redox electrocatalysis" [37] was first introduced by Spiro [38] and Bard [39] and recently summarized. [37] The first practical examples of metallic nanoparticles (NPs) acting as polarized floating electrodes, [40-41] involved the generation of inorganic and organic free radicals aimed at inducing changes in the Fermi level of colloidal metallic NPs (Pt, [42-45] Ag, [46-47] Au [48-49]). Such charged NPs have been used to catalyze dark and photo-induced hydrogen evolution reaction (HER) by means of sacrificial (irreversible) donors such as methylviologen. [39, 42, 44, 49-53] In a recent example of redox photo-electrocatalysis for water oxidation, the electron acceptor/sensitizer $[Ru^{III}(bpy)_3]^{3+}$ was used to oxidize water on iridium oxide NPs. This species was found to be stable for at least few hours and was successfully electrochemically recycled. These experiments were performed in water–acetonitrile (MeCN) mixtures showing the potential of the organic media to enhance the stability of redox shuttles, a common problem in photocatalytic water oxidation systems. [54]

Tetrathiafulvalene (TTF, see chemical structure in Scheme 1) is an organic electron donor exhibiting two reversible and well-separated one-electron oxidation steps. [55-61] The strong self-assembly properties of the radical cation of TTF are involved in the formation of building blocks for the synthesis of highly electrically conducting structures.[59, 62] Such properties have been extensively explored in the fields of organic conductors,[58-59, 61, 63] superconductors,[59, 62, 64] photovoltaic cells,[65] and solar cells,[66] among others.[58, 62] Metal–ligand coordination strategies are widely used to create self-assembled three-dimensional (3D) architectures. TTF-based metal–organic frameworks (MOFs) linked by non-covalent interactions, show an extended charge

transport pathway within the rigid MOF structure, [67-68] where the production of $TTF^{\bullet+}$ sites enhances conductivity, reaching values comparable with those of common organic semiconductors: 10^{-6} $S \cdot cm^{-1}$ for Zn_2(TTFTB) and Co_2(TTFTB) to 10^{-5} $S \cdot cm^{-1}$ for Mn_2(TTFTB) and 10^{-4} $S \cdot cm^{-1}$ for Cd_2(TTFTB) at 298 K where TB stands for tetrabenzoate. [67-68] Recent studies have shown TTF-based conducting polymers to exhibit high electrical conductivity or high charge mobility properties with potential applications in semiconductor and/or optoelectronic devices. [69] The radical cations of derivatives of TTF have been found to dimerize in the solid state, however they need to be stabilized by developing a mechanically bonded interlocked system,[55, 70-71] holding two TTF units within a pre-organized framework,[72-74] or complexing the dimer with a rigid macrocycle. [75] Recently, oxygen evolution by $TTFPF_6$ under illumination with a Xe source (7 W) was reported. [76]

Crystals grown after oxidation of TTF with nitrosonium tetrafluoroborate (**$NOBF_4$**) have been reported to be non-stoichiometric ($(TTF)_3(BF_4)_2$), with TTF moieties stacked in parallel columns arranged into layers alternated with BF_4^- layers. [77] A TTF stack is composed of TTF° monads interspersed with $(TTF^+)_2$ dyads. The conductivity of this salt was found to be $2 \cdot 10^{-5}$ $S \cdot cm^{-1}$, making it a semiconductor. [77]

As an alternative approach to the synthesis of heterojunctions for water oxidation, we report here the *in-situ* self-assembly of TTF, $TTF^{\bullet+}$ and BF_4^- or PF_6^- into p-type semiconductors, which get adsorbed on the surface of Pt microparticles. The self-assembled microrods were noted as [$TTF/TTF^{\bullet+}BF_4^-$]$_n$@Pt and [$TTF/TTF^{\bullet+}PF_6^-$]$_n$@Pt. When photo-irradiated, these semiconducting assemblies were found to trigger water oxidation with the production of O_2 with 100 % efficiency with respect to the initial concentration of $TTF^{\bullet+}$. Pt acts as a floating microelectrode whose Fermi level is imposed by the redox species in solution, injecting electrons from water, into the photo-excited TTF-based assemblies adsorbed on Pt. The different TTF species showed no signs of decomposition in solution, proving their redox reversibility and chemical stability. A gradual increase of the proton concentration in solution results in the protonation of the initial assemblies, and thus, the formation of $HTTF^+$ leads to competing reactions; indeed, $HTTF^+$@Pt has been recently found to photo-reduce H^+ to H_2. [78]

Experimental

Chemical Synthesis of $TTF^{\bullet+}$ by oxidation with $NOBF_4$

The stoichiometric oxidation of TTF (99%, Acros) by $NOBF_4$ (synthesis grade, Merck) was performed entirely inside of a glove box purged with nitrogen (O_2 < 1 ppm, H_2O < 1 ppm). Thus, 0.175 mmol of TTF dissolved in 5 mL of dry MeCN (99.9% extra dry, Sigma Aldrich) were mixed with 0.175 mmol of previously dried $NOBF_4$ dissolved in 5 mL of dry MeCN (Equation 1). The mixture was stirred during 24 h in the dark. Subsequently, the obtained solution was quantitatively transferred to a 25 mL volumetric flask and the volume was completed with dry MeCN. The characterization of the final solution is shown in Figure 1. For the photochemical experiments, an excess of 5% of TTF was used in the synthesis of $TTF^{\bullet+}$ in order to ensure that the reaction was complete and no oxidant was left without reacting, therefore avoiding oxidation of $TTF^{\bullet+}$ to TTF^{2+}. The resulting product in solution was named $TTF/TTF^{\bullet+}BF_4^-$, UV-vis absorption spectra and cyclic voltammograms were recorded in order to verify that TTF^{2+} was not produced. After the completion of the reaction, the solution was thoroughly degassed inside of the glove box in order to evacuate all the NO released during the reaction. The final 7 mM $TTF/TTF^{\bullet+}BF_4^-$ stock solution was always kept inside the glove box and protected from the light. The chemical formation of ions in solution during $TTF^{\bullet+}$ synthesis reads:

$$TTF_{(l)} + NOBF_{4(l)} \rightarrow TTF^{\bullet+}_{(l)} + BF^-_{4(l)} + NO_{(g)} \qquad \text{Eq. 1}$$

Electrochemical Synthesis of $TTF^{\bullet+}$ by Bulk Electrolysis using $BuNPF_6$ as supporting electrolyte.

$TTF^{\bullet+}PF_6^-$ was synthesised by bulk electrolysis in a conventional H-cell with the positive and negative sides separated by glass wool plug avoiding the transfer of $TTF^{\bullet+}$ to the cathodic compartment. The anodic side of the cell was filled with 9.5 mL of 7 mM TTF (0.066 mmol of TTF) and 0.1 M tetrabutylammonium hexafluorophosphate ($BuNPF_6$ > 99.0%, Sigma-Aldrich) in dry MeCN. The cathodic side was filled with 9.5 mL 0.1 M $BuNPF_6$ in dry MeCN. Duocel® reticulated vitreous carbon electrodes, were used as counter and working electrodes, and a Ag/AgCl double-junction was used as organic reference electrode. The solutions

were stirred to increase the rate of mass transport. Before the bulk electrolysis, a cyclic voltammogram was recorded by using a glassy carbon as working electrode in order to determine the potential for the oxidation of TTF (Fig. SI1a in the supporting information, SI). For the electrolysis, the potential of the working electrode was maintained at a constant value of 0.21 V *vs* $TTF^{0/\bullet+}$ until the charge reached a plateau. The final charge corresponds to the number of moles of TTF in the electrochemical cell, with a 100% of Faradaic efficiency (Fig. SI1b). The UV-Vis spectrum of the final $TTF^{\bullet+}PF_6^-$ solution is shown in Fig 1a. For the photocatalytic experiments, 0.0033 mmol of TTF (5 % of the initial amount of TTF) were added to the final solution of $TTF^{\bullet+}PF_6^-$ in order to have the same proportion TTF/ $TTF^{\bullet+}$ reached in the synthesis of $TTF/TTF^{\bullet+}BF_4^-$ (see item above). The product in solution was named $TTF/TTF^{\bullet+}PF_6^-$.

Photosensitized water oxidation reaction (WOR) by $TTF/TTF^{\bullet+}BF_4^-$ and $TTF/TTF^{\bullet+}PF_6^-$

The photosensitized WOR experiments were performed inside the glove box in septum-sealed cells containing 3 mL of suspensions composed of Pt microparticles (<10 μm 99.9%, Aldrich) and $TTF/TTF^{\bullet+}BF_4^-$ or $TTF/TTF^{\bullet+}PF_6^-$ in 20 or 50 % (v/v) water/MeCN mixtures. All solutions were prepared inside the glove box. Water was degassed with N_2 prior insertion to the glove box. The cells were illuminated with a 455 nm Light Emitting Diode (LED, M455L3 Thorlabs) and stirred at 1400 rpm under anaerobic conditions in the glove box at 23 ± 2 ºC. Control reactions without illumination and without Pt were also performed. The evolution of the reaction products was followed by gas chromatography (GC), cyclic voltammetry (CV), UV-Vis spectroscopy, scanning electron microscopy (SEM), X-ray powder diffraction (XRD) and mass spectrometry (MS).

Chemical analysis

The headspace of the septum-sealed glass vials was sampled during the photosensitized WOR by using a lock-in syringe with a push−pull valve (SGE Analytical Sciences). The gas phase was subsequently analysed by injecting it into a Trace 1300 gas chromatograph from Thermo Fisher Scientific, equipped with a thermal conductivity detector (TCD) and a 5 Å molecular sieves (80/100 mesh) column. Argon was used as carrier gas.

It is worth mentioning that before sampling the headspace of the reaction vessels, the solutions were degassed by making vacuum with the sampling syringe; thus, the concentration of dissolved oxygen in solution is significantly lower than that in the headspace and therefore not relevant for the quantification of produced O_2. Prior injection, the line of injection of the GC instrument was purged with N_2 and the exit of the line was connected to a water trap in order to avoid suction of air during the injections.

UV-Visible absorption spectra were taken during the photosensitized WOR by using a 10 mm optical path length quartz cell and a UV-Vis Spectrometer (Agilent Technologies). All the solutions were diluted down to 50 μM prior analysis.

The stability of the TTF species during the reaction was evaluated by electrospray ionization MS (ESI-MS) using a LTQ Velos instrument (Thermo Scientific) equipped with conventional heated ESI source at 2.7 kV potential. The reaction mixture was diluted 10 times with MeCN prior analysis and delivered to the ESI source with flow rate of 5 μL/min. MS analysis was performed in positive polarity with automatic gain control set up to $3e^4$, enhanced scanning mode activated and in *m/z* range of 100 – 1500.

Scanning Electron Microscopy (SEM)

SEM images were obtained by using a FEI Teneo SEM equipped with an EDX detector from Bruker. The sample preparation consisted in drop casting a 30 μL aliquot of the suspension (or solution) on a carbon conductive SEM support. After letting the sample dry completely (1 h) inside the glove box, the holder was immediately transferred to the microscope for analysis. The drying time was the same for all the samples.

X-Ray Powder Diffraction (XRD)

In order to collect enough TTF-based phase for XRD analysis, 1 mL aliquots of TTF/$TTF^{\bullet+}BF_4^-$ and 1 mL aliquots of a suspension composed of TTF/$TTF^{\bullet+}BF_4^-$, water and Pt microparticles after 12 h of photosensitized WOR were dried (inside of the glove box) and subsequently analysed by XRD. Powder diffraction was performed on a Bruker D8 Advance diffractometer using a non-monochromated Cu-source and a LynxEYE 1D detector. Samples were loaded on low background Si-crystal sample holders and spun during measurement.

Electrochemical characterization

Cyclic voltammetric experiments were performed in a three-electrode configuration using a PGSTAT 30 potentiostat (Metrohm, CH). For all the electrochemical analyses Ag and Pt wires were used as pseudo-reference and counter electrodes, respectively. Prior each electrochemical measurement, the microelectrodes were polished with a diamond disk (particle size 0.1μm), washed with MeCN and finally dried in a nitrogen stream. All the solutions and the voltammograms were prepared and recorded in the glove box.

For the characterization of the synthesized $TTF^{\bullet+}$ a carbon microelectrode (diameter = 8 μm) was used as working electrode and 0.1 M tetrabutylammonium hexafluorophosphate ($TBAPF_6$, > 99.0% Sigma Aldrich) was used as supporting electrolyte.

In order to study behaviour of $TTF^{\bullet+}$ in acidic conditions a series of acidified standards were analysed using a Pt microelectrode (diameter = 10 μm) as working electrode. The standard solutions were prepared by adding known concentrations of HBF_4 to 1 mM solutions of $TTF^{\bullet+}$ (in the form of $TTF/TTF^{\bullet+}BF_4^-$) in 20 % (v/v) water/MeCN mixtures. 0.1 M $TBAPF_6$ in 20% (v/v) water/MeCN was used as supporting electrolyte. Fresh solutions were used for each analysis and only the first scan was recorded.

Independently, a cell containing 2 mM $TTF^{\bullet+}$ (in the form of $TTF/TTF^{\bullet+}BF_4^-$) and 1 mg Pt microparticles in 20 % (v/v) water/MeCN mixture was prepared. From this cell, aliquots before and after 10 h of irradiation were taken, diluted twice with the supporting electrolyte, and analysed by cyclic voltammetry. Prior analyses the Pt microparticles were separated by decantation.

Results and discussion

With three absorption maxima at 343, 436 and 582 nm, Figure 1a corroborates the chemical ($TTF^{\bullet+}BF_4^-$) and electrochemical ($TTF^{\bullet+}PF_6^-$) oxidation of TTF to $TTF^{\bullet+}$. [78] No signals associated to the formation of TTF^{2+} or any other compounds were observed. Figure 1b shows the near steady-state cyclic voltammogram obtained after chemical oxidation of TTF, the zero-current in the region around 0.2 V (starting potential) confirms the

total oxidation of TTF. The same voltammogram was obtained upon complete electrochemical oxidation during the synthesis of $TTF^{\bullet+}PF_6^-$ (not shown).

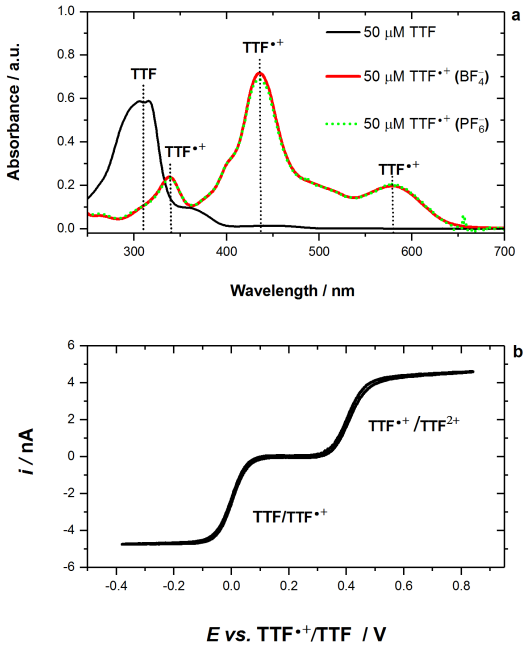

Figure 1. a. UV-vis absorption spectra in dry MeCN of 50 μM TTF and 50 μM $TTF^{\bullet+}$ with BF_4^- and PF_6^- as counter-ions (CI). b. Cyclic voltammogram of 1.0 mM $TTF^{\bullet+}$ (BF_4^- as CI) in dry MeCN (0.1 M $TBAPF_6$ as supporting electrolyte) taken with a 8 μm carbon microelectrode. The scan rate was 25 $mV \cdot s^{-1}$.

Scheme 1. Chemical structure of TTF, $HTTF^+$ and $TTF^{\bullet+}$

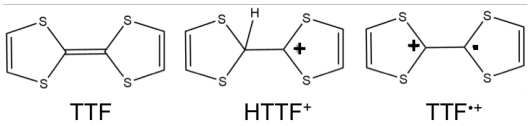

For the photosensitized WOR with $TTF/TTF^{\bullet+}BF_4^-$ or $TTF/TTF^{\bullet+}PF_6^-$ as electron acceptor/photosensitizers in water/MeCN mixtures, the reaction cells were illuminated with a 455 nm LED and stirred at 1400 rpm under anaerobic conditions in the glove box. The LED power, the initial concentration of $TTF^{\bullet+}$ and the amount of Pt microparticles were set to 90.8 $mW \cdot cm^{-2}$, 2 mM, and 1 mg, respectively. The optimisation of these

parameters is summarized in the SI, section SI2. Interestingly, 24 h-aged solutions of TTF/$TTF^{\bullet+}BF_4^-$ and TTF/$TTF^{\bullet+}PF_6^-$ were found to be 30 to 60 % more active than freshly prepared solutions (which will be discussed more in detail in the SEM section), thereafter all the photochemical experiments were performed with 24 h-aged solutions.

In order to study the effect of the water content on the performance of $TTF^{\bullet+}$, photo-irradiation in 20 % (v/v) and 50 % (v/v) water/MeCN mixtures were performed. As shown in the gas chromatograms in Figure 2, oxygen is produced by the photosensitized WOR by both, TTF/$TTF^{\bullet+}BF_4^-$ and TTF/$TTF^{\bullet+}PF_6^-$ (no other electrolyte involved in the reaction) and Pt microparticles. Control reactions in the dark with Pt, and under irradiation without Pt did not yield O_2 indicating that the oxygen generation by $TTF^{\bullet+}$ requires both light and Pt microparticles.

Figure 2 shows that in 20% (v/v) water/MeCN mixtures the evolution of O_2 by photo-excitation of TTF/$TTF^{\bullet+}BF_4^-$ or TTF/$TTF^{\bullet+}PF_6^-$ reaches a maximum after 10 h of reaction with an efficiency of about 70 % with respect to the initial concentration of $TTF^{\bullet+}$ (details of the calculation in Section SI2). In contrast, in 50% water/MeCN mixtures, both, TTF/$TTF^{\bullet+}BF_4^-$ and TTF/$TTF^{\bullet+}PF_6^-$ yield O_2 with 100% efficiency within 20 h of reaction. Thereafter, the concentration of O_2 starts to decline due to O_2 reduction. After 48 h of photo-reaction about 20 nmoles of H_2, (accounting for < 1 % efficiency) were also detected due to proton reduction. Indeed, the formation of protons during the WOR leads to the formation of $HTTF^+$. Both, the selective reduction of O_2 to H_2O by $HTTF^+$ in acidic media in the dark (Eq. SI3) [79] and the reduction of protons on Pt by photo-excited $HTTF^+$ (Eqs. SI4 to SI6), [78] have been previously reported. It should be noted that the reduction of protons by photo-excited $HTTF^+$ is more efficient at proton concentrations higher than 10^{-1} M and in presence of a strong acid. [78] Therefore, the slow and inefficient H_2 evolution observed in this work is due to the low proton concentration, which is never higher than 10^{-3} M as shown by CV (*vide infra*). From a safety standpoint, there is not risk of mixing H_2 and O_2 in this experiment as H_2 is produced in trace amounts (< 20 nmole).

All in all, the WOR by photo-excited $TTF^{\bullet+}$ can be summarised as:

$$4TTF^{\bullet+} + 2H_2O \xrightarrow[Pt,h\nu]{} 4TTF + O_2 + 4H^+ \qquad \text{Eq. 2}$$

The TTF molecules formed can be further protonated to form $HTTF^+$.

Figure 2 also shows that the nature of the anion does not play a relevant role in the photo-activation of $TTF^{\bullet+}$, as the evolution of O_2 by both $TTF/TTF^{\bullet+}BF_4^-$ and $TTF/TTF^{\bullet+}PF_6^-$ proved to be the same.

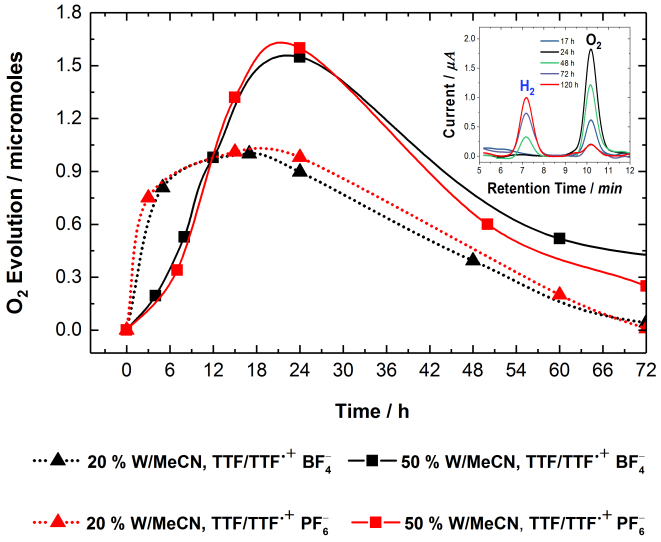

Figure 2. Gas evolution during photosensitized WOR. Initial conditions: 2 mM $TTF^{\bullet+}$ and 1 mg Pt (< 10 μm) in 20% v/v (dotted lines) and 50 % v/v (full lines) water/MeCN (W/MeCN) mixtures. Black and red plots correspond to the photocatalytic experiments performed with $TTF/TTF^{\bullet+}BF_4^-$ and $TTF/TTF^{\bullet+}PF_6^-$, respectively. All the samples were vigorously stirred and irradiated with a 455 nm LED. Inset: chromatograms obtained at after different times of the WOR by $TTF/TTF^{\bullet+}BF_4^-$ in 50 % (v/v) water/MeCN mixtures. Even though the amount of O_2 detected is 50 times higher than that of H_2, the signal associated to H_2 is comparable to that of O_2 due to the detection method. Indeed, the difference in thermal conductivity between H_2 and Ar (carrier gas) is 20 times higher than that between O_2 and Ar, accounting for a higher sensitivity for the detection of H_2.

Considering that the concentration of protons increased as the WOR progressed, cyclic voltammetry was used to study the behaviour of $TTF^{\bullet+}$ in acidic conditions (Fig. 3). As described in detail in the experimental section, a series of acidified $TTF/TTF^{\bullet+}BF_4^-$ standards were analysed by cyclic voltammetry using a Pt microelectrode (diameter = 10 μm) as working electrode. Such configuration closely mimics the TTF-based

photosensitized WOR system reported in this work where 10 µm Pt microparticles were used as electrocatalysts. Independently, aliquots before and after 10 h of irradiation, of a suspension containing 2 mM $TTF^{\bullet+}$ (in the form of $TTF/TTF^{\bullet+}BF_4^-$) and 1 mg Pt microparticles in 20 % (v/v) water/MeCN, were also analysed by cyclic voltammetry (Fig. SI2a).

All the voltammograms in Figure 3 show two characteristic one-electron steady-state voltammetric signals associated to the $TTF^{\bullet+}/TTF$ and $TTF^{2+}/TTF^{\bullet+}$ redox couples. The potential window using the Pt microelectrode is limited by the reduction of protons in the negative side and the oxidation of water in the positive side. The wave observed between the reduction of protons and the reduction of $TTF^{\bullet+}$ corresponds to O_2 reduction as confirmed by the $[H^+]=1.8\cdot10^{-2}$ M standard, which prior electrochemical analysis was saturated with O_2 (see section SI4 for more details, Fig. SI2b). The sharp peak observed on the return anodic sweep after the reduction of $TTF^{\bullet+}$ to TTF (0.55 V *vs* SHE) indicates the adsorption of $TTF/TTF^{\bullet+}$ assemblies on the surface of the Pt microelectrode (as confirmed by SEM for Pt microparticles *vide infra*). The scan rate dependence analysis of the deposits on the electrode was inconclusive as the deposit-related signals obtained after repolishing the electrode in between each scan were not reproducible.

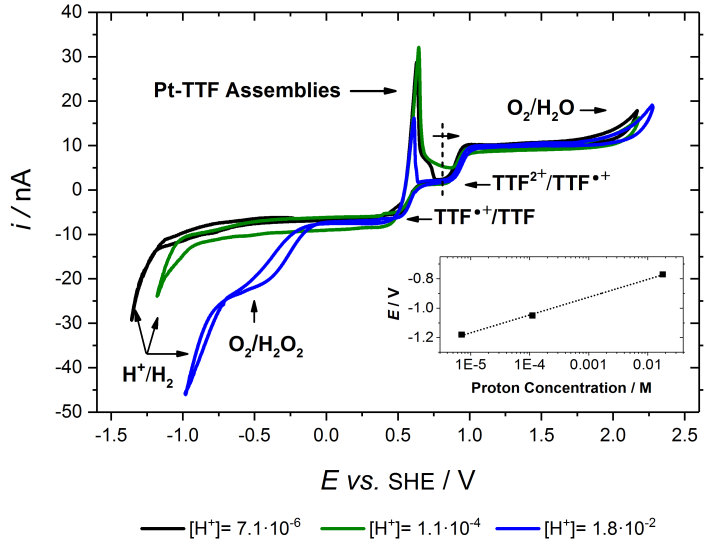

Figure 3. Cyclic voltammograms of acidified standards of 1 mM $TTF^{\bullet+}$ (in the form of $TTF/TTF^{\bullet+}BF_4^-$) in 20% water/MeCN. Concentration of HBF_4: $7.1\cdot10^{-6}$ M, $1.1\cdot10^{-4}$ M and $1.8\cdot10^{-2}$ M. Potential scan: 0.82 V (vertical dashed line) to 2.3 V, followed by 2.3 V to negative potentials and back to 0.75 V. Inset figure: *E* (onset potential for proton reduction) *vs* $\log_{10}[H^+]$.

The onset potential for proton reduction dependence *vs* $\log_{10}[H^+]$ for the acidified $TTF^{\bullet+}$ standards, is linear with a slope of 0.121 V (inset Fig. 3), which accounts for a 2:1 H^+/e^- ratio. This behavior is due to the coupled reduction of protons by the Pt electrode and $HTTF^+$, which is explained in detail in Section SI4.

Using this electrochemical proton calibration, the proton concentration of the sample taken after 10 h of photosensitized WOR (Fig. SI2a) was estimated to be $1.4\cdot10^{-3}$ M (4.3 μmoles of protons) that in accordance with Eq. 2 corresponds to 1.1 μmoles of produced O_2, which is indeed the amount of O_2 detected by GC after 10 h of reaction (1 μmol, doted black line, Fig. 2). This analysis therefore corroborates the 4:1 ratio (H^+: O_2) expected for the photosensitized WOR described in Eq. 2.

SEM and EDX images were taken at different moments of the photosensitized WOR (Fig. 4). The images corresponding to the samples prepared from fresh $TTF^{\bullet+}$ solutions (without Pt) displayed no features (not shown), while the samples aged during 24 h (in the dark, without Pt), showed flower-like assemblies of about 50 μm size formed from cubic assemblies of between 5 and 25 μm (Fig. 4a). As demonstrated by the EDX analysis, such assemblies are composed of S and C, indicating that they are TTF-based. As a matter of fact, the synthesis of a mixed-valence (MV) dyad between TTF and $TTF^{\bullet+}$ ($(TTF/TTF)^{\bullet+}$) and the π-dimer $(TTF^{\bullet+})_2$, has been previously reported. [80] Such studies suggest that the self-assemblies formed in this work result from the interaction between TTF and $TTF^{\bullet+}$. Indeed, we observed that $TTF^{\bullet+}$ solutions in the dark slowly disproportionate, thereby generating more TTF available for self-assembly. Such TTF-based self-assemblies result from weak intermolecular interactions: van der Waals, CT interaction and π-π stacking. [80-81] [82]

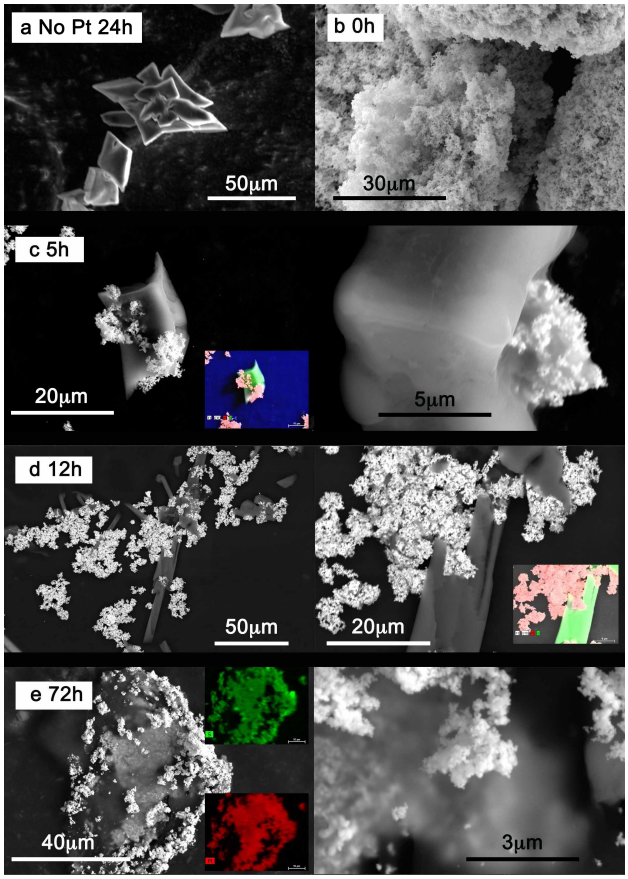

Figure 4. SEM images of TTF-based assemblies during photosensitized WOR. Conditions: $[TTF^{\bullet+}]_0$= 2mM (in the form of $TTF/TTF^{\bullet+}BF_4^-$), Pt=1mg, 50% (v/v) water/MeCN. 30 µL aliquots were dried on carbon paste inside the glove box. The drying time was 1 h for all the samples. The inset figures are EDX images showing the distribution of sulfur (green) and Pt (red). a. $TTF^{\bullet+}$ aged during 24 h in absence of Pt and in dark. WOR progression in time: b. 0h; c. 5h; d. 12h; e. 72h. The images on the right of Figures 4.c, d, and e are close-ups of the corresponding images on the left.

As mentioned above, the $[TTF/TTF^{\bullet+}BF_4^-]_n$@Pt assemblies formed from fresh $TTF/TTF^{\bullet+}BF_4^-$ solutions were found to be between 30 and 60% less active than assemblies from solutions aged during 24h, indicating that the flower-liked self-assemblies observed in Figure 4a are the precursors for more photo-active TTF-based assemblies.

The morphology of the TTF-based assemblies on the Pt particles was found to change dynamically as the water oxidation progressed. For comparison, images taken prior illumination (Fig. 4b) showed only Pt particles.

After 5 h of irradiation (Fig. 4c) the SEM and EDX images showed TTF-based rods of about 30 μm long and 15 μm width growing on the Pt microparticles, which correlates with the sharp peak observed when analysing $TTF/TTF^{\bullet+}BF_4^-$ by cyclic voltammetry on a Pt microelectrode. Similar TTF-based assemblies on Pt have been previously reported by Penner *et al.* [83], where crystalline $TTF(Br)_x$ was obtained by slow electrochemical oxidation of TTF in a bromide-containing electrolyte by a Pt NP-modified graphite electrode. The crystalline $TTF(Br)_x$ structure consisted of **π-π** stacks of $TTF^{\bullet+}$ electron acceptors arranged in parallel to an equal number of (incomplete) rows of Br^- electron donors (hence the sub index) .[84] In such structure, electrons were delocalized along the $TTF^{\bullet+}$ **π-π** stacks that were in turn arrayed along the *c*-axis of the crystal, with higher conductivity along the *c*-axis compared to the perpendicular direction. This fact also explains the crystal preferential growth along the *c*-axis, resulting in long, narrow arrays.[84] Interestingly in ref 84, physisorbed TTF, was found to be crucial for the nucleation of the $(TTF)Br_x$ nanocrystals, which is in line with the observation that assemblies between $TTF^{\bullet+}$ and TTF physisorbed on Pt particles, are the nucleus for larger assemblies and, therefore the starting point for the photosensitised WOR described here.

After 12-24 h of reaction (Fig. 4d), the SEM and EDX images showed dense TTF-based rods as long as 150 μm. This corresponds to the maximum of O_2 production shown in Fig. 2. For further corroboration, SEM and EDX images of dried aliquots of the $[\ TTF/TTF^{\bullet+}PF_6^-\ ]_n$@Pt system were also taken, revealing the same kind of microrods (Fig. SI3a). By 72 h (Fig. 4e), the TTF-based microrods had been replaced by amorphous and less dense assemblies. A corresponding close-up image (on the right) showed TTF-based film-like assemblies covering the Pt particles.

SEM and EDX images of dried aliquots of $TTF^{\bullet+}$ stirred during 72 h under irradiation (without Pt), showed cubic assemblies 10 μm long and 10 μm width (Fig. SI3b), which are completely different from the morphology observed in Fig. 4e (same time of illumination in a reaction containing Pt). This indicates that the presence of Pt not only affects the activity of the composites but also their morphology and dimensions. It is important to note that the Fermi level of the Pt microparticles is constantly tuned by the composition of the TTF-based assemblies. [37]

In order to assess structural differences in the [TTF/TTF$^{\bullet+}$BF$_4^-$]$_n$@Pt assemblies during the photosensitised WOR, 1 mL aliquots of TTF/TTF$^{\bullet+}$BF$_4^-$ and 1 mL aliquots of [TTF/TTF$^{\bullet+}$BF$_4^-$]$_n$@Pt in 20 % v/v water/MeCN after 12 h of photosensitized WOR, were dried out (inside of the glove box) and subsequently analysed by XRD (Fig. SI4). Bragg scattering does occur for both samples. It was attempted to model the data by Rietveld refinement using the only structural model reported for $(TTF)_3(BF_4)_2$. [77] However, the resulting fit did not provide unambiguous proof for the presence of $(TTF)_3(BF_4)_2$, at least not of the reported polymorph. The XRD pattern of the sample obtained after 12 h of photosensitized WOR, shows lesser crystallinity than that of the sample before reaction and a modified phase composition, with the signals corresponding to the Pt microparticles dominating the spectrum at $2\theta > 38$. A change in phase composition is expected considering that after photosensitized WOR the system contains TTF, TTF$^+$ and HTTF$^+$, which, as explained before, are likely to interact with each other, yielding a different packing than that reported for those three species independently. As a conclusion, the XRD characterization clearly shows a change in phase composition during the photosensitized WOR, but due to the complexity of the system, a structural model could not be assigned to the diffraction patterns.

In accordance with the concept of redox electrocatalysis on electrically floating metallic particles, [37] the most plausible mechanism for the water oxidation by these photo-excited [TTF/TTF$^{\bullet+}$]$_n$@Pt assemblies is shown in the energy diagram illustrated in Scheme 2: In the dark, the Fermi level of the electrons on the Pt microparticles is determined by the Nernst potential of the redox species in excess in solution, *i.e.* TTF/TTF$^{\bullet+}$, at about 0.55V *vs* SHE; which is too low to trigger water oxidation. This corresponds to a Fermi level at –4.95 eV assuming that the origin of the standard redox potential scale corresponds to –4.4 eV. However, upon illumination the [TTF/TTF$^{\bullet+}$]$_n$@Pt assemblies are photo-excited, leaving low energy holes able to accept electrons from the Pt particle, which in turn can oxidise water on its surface thereby producing O_2 and H^+. Indeed, the redox potential of the photo-excited assemblies is higher than 2.5 V *vs* SHE considering that the photon energy of excitation is 2.7 eV. As shown in Scheme 2, the illumination results in a lowering of the Fermi energy of the Pt microparticles (more negative than –7 eV) well below the Nernst potential for water oxidation.

As the reduction of $[TTF/TTF^{\bullet+}]_n$@Pt proceeds, the amount of the sensitizer $TTF^{\bullet+}$ decreases and the TTF formed becomes protonated (Eq. SI4). As shown previously, the redox potential of $HTTF^{+}$ is in turn capable of reducing oxygen in the dark. [78]

Scheme 2. Simplified energy scheme involved in the photosensitized WOR by $TTF^{\bullet+}$ in presence of Pt microparticles.

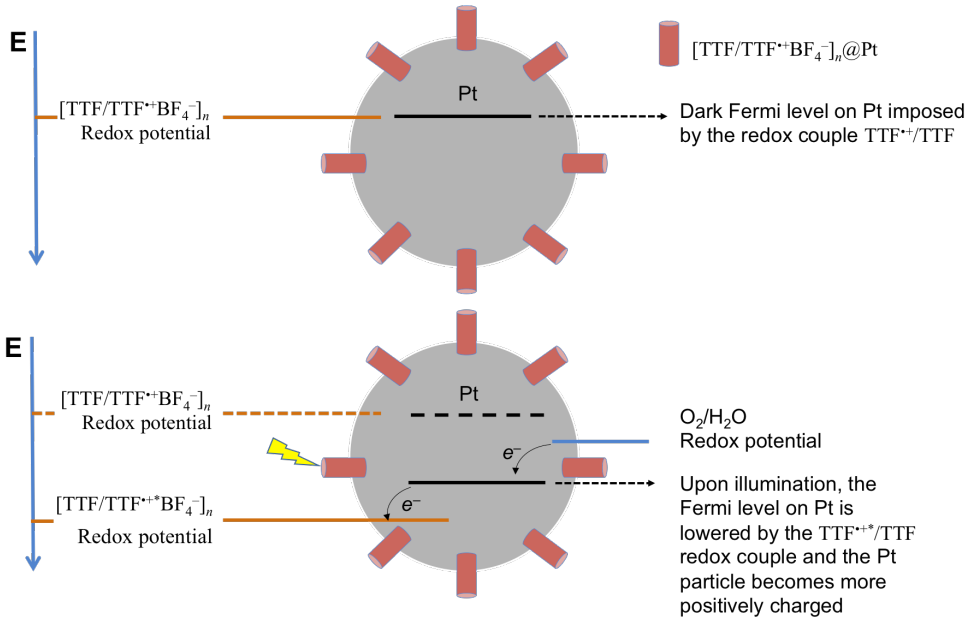

The stability of the TTF species in solution during the photochemical reaction was studied by UV-Vis absorption and MS. Figure 5 shows the gradual and complete reduction of $TTF^{\bullet+}$ to TTF during the photosensitized WOR. No absorption signals other than those corresponding to TTF and $TTF^{\bullet+}$ are observed indicating the absence of decomposition of $TTF^{\bullet+}$ during the photochemical reaction. In addition, the MS spectra obtained at different times of reaction (Fig. SI5), showed no decomposition products, meaning no *m*/*z* signals associated to the opening of the TTF rings. This accounts as evidence for the stability of the TTF species and their involvement in the reaction not as sacrificial electron acceptors/donors, but as reversible redox shuttle.

The complete reduction of $TTF^{\bullet+}$ to TTF is an important advantage of the photosensitized WOR system reported in this work. As previously discussed, TTF was found to photo-reduce protons to hydrogen, oxidizing

TTF back to $TTF^{\bullet+}$,[78] which would ultimately reset the WOR system, making the whole cycle sustainable as all the products of the reaction are reusable.

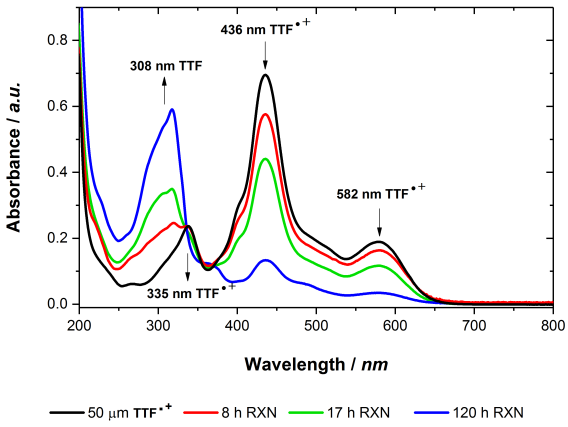

Figure 5. UV-Visible absorption spectra taken during photosensitized WOR by $TTF^{\bullet+}$ (in the form of $TTF/TTF^{\bullet+}BF_4^-$). Initial conditions for the reaction: $[TTF^{\bullet+}]_0$: 2mM, 50% (v/v) water/MeCN, 1 mg of Pt (<10μm), irradiation at 455 nm. All the solutions were diluted down to 50 μM with dry MeCN inside the glove box prior analysis.

Conclusions

In summary, we report photosensitized water oxidation by self-assembled $[TTF/TTF^{\bullet+}]_n$@Pt in water-MeCN mixtures. The efficiency of the photosensitized WOR towards O_2, H^+ and TTF, was found to be 100 % with respect to the initial concentration of $TTF^{\bullet+}$. Pt microparticles act as floating microelectrodes whose Fermi level is imposed by the redox species in solution, here predominantly $TTF^{\bullet+}/TTF$. Thus, Pt oxidises water after injection of electrons into the photo-excited $TTF^{\bullet+}$-based semiconducting assemblies that act as both electron acceptors and photosensitizers. A gradual increase of the proton concentration in solution leads to the protonation of the assemblies, which shifts the Pt Fermi level to more negative values. Although the process is slow, the initial electron acceptor/photosensitizer $TTF^{\bullet+}$ showed no signs of decomposition in solution, proving its redox reversibility and chemical stability, and therefore its potential to be used as a redox shuttle for water oxidation. More suitable derivatives of $TTF^{\bullet+}$ (Section SI8) and more environmentally friendly and less expensive catalysts are being currently evaluated in order to improve the kinetics of the reaction.

All in all, this work opens a new avenue for water photo-oxidation based on the design of self-assembled organic p-type semiconductors, which are shown to be efficient at accepting electrons from an electrocatalyst

particle and driving water oxidation. Considering the capability of photoexcited $HTTF^{+}$ to reduce protons on Pt microparticles, the next step towards the development of a complete and sustainable artificial photosynthetic system is the efficient separation of protons from the WOR medium. Thus, protons can be reduced by TTF in a separated compartment, and the $TTF^{\bullet+}$ formed during the reduction of protons can in turn be used to oxidise more water. The fact that both, TTF and $TTF^{\bullet+}$ can be electrochemically recycled due to their stability and reversibility can be also exploited in order to make a more flexible artificial photosynthetic device.

Associated Content

The supporting information is available free of charge on the ACS Publications website at DOI:

Electrochemical synthesis of $TTF^{\bullet+}$, optimization of the photosensitised WOR, oxygen and proton reduction by $HTTF^{+}$, electrochemical characterization of TTF/ $TTF^{\bullet+}BF_4^{-}$, SEM-EDX, XRD, MS and description of TTF derivatives.

Acknowledgements

The authors wish to acknowledge the Swiss Science Foundation SNSF grant 200021_175745 entitled: Photo Induced Charge Transfer Reaction at Molecular Interfaces: Towards new routes of solar energy storage. V.C.B. thank the SNSF Ambizione Energy Project No. 154297. We thank Dr. Pascal Schouwink and Dr. Emad Oveisi for helpful discussions.

References

1. Li, Z.; Wang, W.; Ding, C.; Wang, Z.; Liao, S.; Li, C., Biomimetic Electron Transport Via Multiredox Shuttles From Photosystem II To A Photoelectrochemical Cell For Solar Water Splitting. *Energy Environ. Sci.* **2017,** *10* (3), 765-771.

2. Hisatomi, T.; Kubota, J.; Domen, K., Recent Advances In Semiconductors For Photocatalytic And Photoelectrochemical Water Splitting. *Chem. Soc. Rev.* **2014,** *43* (22), 7520-7535.

3. Meyer, K.; Ranocchiari, M.; van Bokhoven, J. A., Metal Organic Frameworks For Photo-Catalytic Water Splitting. *Energy Environ. Sci.* **2015,** *8* (7), 1923-1937.

4. Yu, Z.; Li, F.; Sun, L., Recent Advances In Dye-Sensitized Photoelectrochemical Cells For Solar Hydrogen Production Based On Molecular Components. *Energy Environ. Sci.* **2015,** *8* (3), 760-775.

5. Moniz, S. J. A.; Shevlin, S. A.; Martin, D. J.; Guo, Z.-X.; Tang, J., Visible-Light Driven Heterojunction Photocatalysts For Water Splitting - A Critical Review. *Energy Environ. Sci.* **2015,** *8* (3), 731-759.

6. Deng, X.; Tüysüz, H., Cobalt-Oxide-Based Materials as Water Oxidation Catalyst: Recent Progress and Challenges. *ACS Catal.* **2014,** *4* (10), 3701-3714.

7. Kärkäs, M. D.; Verho, O.; Johnston, E. V.; Åkermark, B., Artificial Photosynthesis: Molecular Systems for Catalytic Water Oxidation. *Chem. Rev.* **2014,** *114* (24), 11863-12001.

8. Frischmann, P. D.; Mahata, K.; Wurthner, F., Powering The Future Of Molecular Artificial Photosynthesis With Light-Harvesting Metallosupramolecular Dye Assemblies. *Chem. Soc. Rev.* **2013,** *42* (4), 1847-1870.

9. Young, K. J.; Martini, L. A.; Milot, R. L.; Snoeberger Iii, R. C.; Batista, V. S.; Schmuttenmaer, C. A.; Crabtree, R. H.; Brudvig, G. W., Light-Driven Water Oxidation For Solar Fuels. *Coord. Chem. Rev.* **2012,** *256* (21–22), 2503-2520.

10. Hara, M.; Lean, J. T.; Mallouk, T. E., Photocatalytic Oxidation of Water by Silica-Supported Tris(4,4‘-dialkyl-2,2‘-bipyridyl)ruthenium Polymeric Sensitizers and Colloidal Iridium Oxide. *Chem. Mater.* **2001,** *13* (12), 4668-4675.

11. Yamazaki, H.; Shouji, A.; Kajita, M.; Yagi, M., Electrocatalytic And Photocatalytic Water Oxidation To Dioxygen Based On Metal Complexes. *Coord. Chem. Rev.* **2010,** *254* (21), 2483-2491.

12. Dismukes, G. C.; Brimblecombe, R.; Felton, G. A. N.; Pryadun, R. S.; Sheats, J. E.; Spiccia, L.; Swiegers, G. F., Development of Bioinspired Mn_4O_4−Cubane Water Oxidation Catalysts: Lessons from Photosynthesis. *Acc. Chem. Res.* **2009,** *42* (12), 1935-1943.

13. Zong, R.; Thummel, R. P., A New Family of Ru Complexes for Water Oxidation. *J. Am. Chem. Soc.* **2005,** *127* (37), 12802-12803.

14. Sartorel, A.; Carraro, M.; Toma, F. M.; Prato, M.; Bonchio, M., Shaping The Beating Heart Of Artificial Photosynthesis: Oxygenic Metal Oxide Nano-Clusters. *Energy Environ. Sci.* **2012,** *5* (2), 5592-5603.

15. Xu, Y.; Fischer, A.; Duan, L.; Tong, L.; Gabrielsson, E.; Åkermark, B.; Sun, L., Chemical And Light-Driven Oxidation Of Water Catalyzed By An Efficient Dinuclear Ruthenium Complex. *Angew. Chem., Int. Ed. Engl.* **2010,** *49* (47), 8934-8937.

16. Concepcion, J. J.; Jurss, J. W.; Templeton, J. L.; Meyer, T. J., One Site is Enough. Catalytic Water Oxidation by $[Ru(tpy)(bpm)(OH_2)]^{2+}$ and $[Ru(tpy)(bpz)(OH_2)]^{2+}$. *J. Am. Chem. Soc.* **2008,** *130* (49), 16462-16463.

17. Robinson, D. M.; Go, Y. B.; Greenblatt, M.; Dismukes, G. C., Water Oxidation by λ-MnO_2: Catalysis by the Cubical Mn_4O_4 Subcluster Obtained by Delithiation of Spinel $LiMn_2O_4$. *J. Am. Chem. Soc.* **2010,** *132* (33), 11467-11469.

18. Wada, T.; Tsuge, K.; Tanaka, K., Electrochemical Oxidation of Water to Dioxygen Catalyzed by the Oxidized Form of the Bis(ruthenium – hydroxo) Complex in H_2O. *Angew. Chem., Int. Ed. Engl.* **2000,** *39* (8), 1479-1482.

19. Su, J.; Guo, L.; Bao, N.; Grimes, C. A., Nanostructured $WO_3/BiVO_4$ Heterojunction Films for Efficient Photoelectrochemical Water Splitting. *Nano Lett.* **2011,** *11* (5), 1928-1933.

20. Saito, R.; Miseki, Y.; Sayama, K., Highly Efficient Photoelectrochemical Water Splitting Using A Thin Film Photoanode Of $BiVO_4/SnO_2/WO_3$ Multi-Composite In A Carbonate Electrolyte. *Chemical Communications* **2012,** *48* (32), 3833-3835.

21. Hong, S. J.; Lee, S.; Jang, J. S.; Lee, J. S., Heterojunction $BiVO_4/WO_3$ Electrodes For Enhanced Photoactivity Of Water Oxidation. *Energy Environ. Sci.* **2011,** *4* (5), 1781-1787.

22. Pihosh, Y.; Turkevych, I.; Mawatari, K.; Asai, T.; Hisatomi, T.; Uemura, J.; Tosa, M.; Shimamura, K.; Kubota, J.; Domen, K.; Kitamori, T., Nanostructured $WO_3/BiVO_4$ Photoanodes for Efficient Photoelectrochemical Water Splitting. *Small* **2014,** *10* (18), 3692-3699.

23. Pilli, S. K.; Deutsch, T. G.; Furtak, T. E.; Brown, L. D.; Turner, J. A.; Herring, A. M., $BiVO_4/CuWO_4$ Heterojunction Photoanodes For Efficient Solar Driven Water Oxidation. *Phys. Chem. Chem. Phys.* **2013,** *15* (9), 3273-3278.

24. Zhang, L.; Reisner, E.; Baumberg, J. J., Al-Doped ZnO Inverse Opal Networks As Efficient Electron Collectors In $BiVO_4$ Photoanodes For Solar Water Oxidation. *Energy Environ. Sci.* **2014,** *7* (4), 1402-1408.

25. Fu, X.; Xie, M.; Luan, P.; Jing, L., Effective Visible-Excited Charge Separation in Silicate-Bridged $ZnO/BiVO_4$ Nanocomposite and Its Contribution to Enhanced Photocatalytic Activity. *ACS Appl. Mater. Interfaces* **2014,** *6* (21), 18550-18557.

26. Ho-Kimura, S.; Moniz, S. J. A.; Handoko, A. D.; Tang, J., Enhanced Photoelectrochemical Water Splitting By Nanostructured $BiVO_4$–TiO_2 Composite Electrodes. *J. Mater. Chem. A* **2014,** *2* (11), 3948-3953.

27. Hou, Y.; Zuo, F.; Dagg, A.; Feng, P., A Three-Dimensional Branched Cobalt-Doped α-Fe_2O_3 Nanorod/$MgFe_2O_4$ Heterojunction Array as a Flexible Photoanode for Efficient Photoelectrochemical Water Oxidation. *Angew. Chem. Int. Ed. Engl.* **2013,** *52* (4), 1248-1252.

28. Sivula, K.; Formal, F. L.; Grätzel, M., WO_3−Fe_2O_3 Photoanodes for Water Splitting: A Host Scaffold, Guest Absorber Approach. *Chem. Mater.* **2009,** *21* (13), 2862-2867.

29. Bora, D. K.; Braun, A.; Erni, R.; Müller, U.; Döbeli, M.; Constable, E. C., Hematite–NiO/α-$Ni(OH)_2$ Heterostructure Photoanodes With High Electrocatalytic Current Density And Charge Storage Capacity. *Phys. Chem. Chem. Phys.* **2013,** *15* (30), 12648-12659.

30. Li, J.; Meng, F.; Suri, S.; Ding, W.; Huang, F.; Wu, N., Photoelectrochemical Performance Enhanced By A Nickel Oxide–Hematite P–N Junction Photoanode. *Chem. Commun.* **2012,** *48* (66), 8213-8215.

31. Li, W.; Sheehan, S. W.; He, D.; He, Y.; Yao, X.; Grimm, R. L.; Brudvig, G. W.; Wang, D., Hematite-Based Solar Water Splitting in Acidic Solutions: Functionalization by Mono- and Multilayers of Iridium Oxygen-Evolution Catalysts. *Angew. Chem. Int. Ed. Engl.* **2015,** *54* (39), 11428-11432.

32. McDonald, K. J.; Choi, K.-S., Synthesis and Photoelectrochemical Properties of $Fe_2O_3/ZnFe_2O_4$ Composite Photoanodes for Use in Solar Water Oxidation. *Chem. Mater.* **2011,** *23* (21), 4863-4869.

33. Kim, W.; Tachikawa, T.; Monllor-Satoca, D.; Kim, H.-i.; Majima, T.; Choi, W., Promoting Water Photooxidation On Transparent WO_3 Thin Films Using An Alumina Overlayer. *Energy Environ. Sci.* **2013,** *6* (12), 3732-3739.

34. Ma, S. S. K.; Maeda, K.; Abe, R.; Domen, K., Visible-Light-Driven Nonsacrificial Water Oxidation Over Tungsten Trioxide Powder Modified With Two Different Cocatalysts. *Energy Environ. Sci.* **2012,** *5* (8), 8390-8397.

35. Bi, Y.; Ouyang, S.; Cao, J.; Ye, J., Facile Synthesis Of Rhombic Dodecahedral AgX/Ag_3PO_4 (X = Cl, Br, I) Heterocrystals With Enhanced Photocatalytic Properties And Stabilities. *Phys. Chem. Chem. Phys.* **2011,** *13* (21), 10071-10075.

36. Lin, Y.-G.; Hsu, Y.-K.; Chen, Y.-C.; Wang, S.-B.; Miller, J. T.; Chen, L.-C.; Chen, K.-H., Plasmonic $Ag@Ag_3(PO_4)1-x$ Nanoparticle Photosensitized ZnO Nanorod-Array Photoanodes For Water Oxidation. *Energy Environ. Sci.* **2012,** *5* (10), 8917-8922.

37. Peljo, P.; Scanlon, M. D.; Olaya, A. J.; Rivier, L.; Smirnov, E.; Girault, H. H., Redox Electrocatalysis of Floating Nanoparticles: Determining Electrocatalytic Properties without the Influence of Solid Supports. *J. Phys. Chem. Lett.* **2017,** *8* (15), 3564-3575.

38. Spiro, M., Heterogeneous Catalysis in Solution. Part 17.-Kinetics of Oxidation-Reduction Reaction Catalysed by Electron Transfer through the Solid: An Electrochemical Treatment. *J. Chem. Soc., Faraday Trans. 1* **1979,** *75*, 1507.

39. Miller, D. S.; Bard, A. J.; McLendon, G.; Ferguson, J., Catalytic Water Reduction at Colloidal Metal "microelectrodes". 2. Theory and Experiment. *J. Am. Chem. Soc.* **1981,** *103* (18), 5336.

40. Henglein, A., Small-Particle Research: Physicochemical Properties of Extremely Small Colloidal Metal and Semiconductor Particles. *Chem. Rev.* **1989,** *89* (8), 1861.

41. Henglein, A., Physicochemical Properties of Small Metal Particles in Solution: "microelectrode" reactions, Chemisorption, Composite Metal Particles, and the Atom-to-Metal Transition. *J. Phys. Chem.* **1993,** *97* (21), 5457.

42. Venturi, M.; Mulazzani, Q. G.; Hoffman, M. Z., Radiolytically Induced One-Electron Reduction of Methylviologen in Aqueous Solution. Platinum-Catalyzed Formation of Dihydrogen. *J. Phys. Chem.* **1984,** *88* (5), 912.

43. Miller, D. S.; McLendon, G., Quantitative Electrochemical Kinetics Studies Of "microelectrodes": Catalytic Water Reduction by Methyl Viologen/colloidal Platinum. *J. Am. Chem. Soc.* **1981,** *103* (23), 6791.

44. Grätzel, C. K.; Grätzel, M., Hydrogen Evolution from the Photolysis of Alcoholic Benzophenone Solutions via Redox Catalysis. *J. Am. Chem. Soc.* **1979,** *101* (26), 7741.

45. Kiwi, J.; Grätzel, M., Projection, Size Factors, and Reaction Dynamics of Colloidal Redox Catalysts Mediating Light Induced Hydrogen Evolution from Water. *J. Am. Chem. Soc.* **1979,** *101* (24), 7214.

46. Henglein, A., Catalysis of Hydrogen Formation from an Organic Radical in Aqueous Solutions by Colloidal Silver. *Angew. Chem., Int. Ed. Engl.* **1979,** *18* (5), 418.

47. Henglein, A.; Lilie, J., Storage of Electrons in Aqueous Solution: The Rates of Chemical Charging and Discharging the Colloidal Silver Microelectrode. *J. Am. Chem. Soc.* **1981,** *103* (5), 1059.

48. Meisel, D., Catalysis of Hydrogen Production in Irradiated Aqueous Solutions by Gold Sols. *J. Am. Chem. Soc.* **1979,** *101* (20), 6133.

49. Meisel, D.; Mulac, W. A.; Matheson, M. S., Catalysis of Methyl Viologen Radical Reactions by Polymer-Stabilized Gold Sols. *J. Phys. Chem.* **1981,** *85* (2), 179.

50. Henglein, A., Catalysis of the Reduction of thallium(1+) and of Dichloromethane by Colloidal Silver in Aqueous Solution. *J. Phys. Chem.* **1979,** *83* (22), 2858.

51. Henglein, A.; Lindig, B.; Westerhausen, J., Photochemical Electron Storage on Colloidal Metals and Hydrogen Formation by Free Radicals. *J. Phys. Chem.* **1981,** *85* (12), 1627.

52. Aslan, E.; Akin, I.; Patir, I. H., Enhanced Hydrogen Evolution Catalysis Based on Cu Nanoparticles Deposited on Carbon Nanotubes at the Liquid/Liquid Interface. *ChemCatChem* **2016,** *8* (4), 719.

53. Ozel, F.; Aslan, E.; Sarilmaz, A.; Hatay Patir, I., Hydrogen Evolution Catalyzed by Cu_2WS_4 at Liquid–Liquid Interfaces. *ACS Appl. Mater. Interfaces* **2016,** *8* (39), 25881.

54. Hidalgo-Acosta, J. C.; Méndez, M. A.; Scanlon, M. D.; Vrubel, H.; Amstutz, V.; Adamiak, W.; Opallo, M.; Girault, H. H., Catalysis Of Water Oxidation In Acetonitrile By Iridium Oxide Nanoparticles. *Chem. Sci.* **2015,** *6* (3), 1761-1769.

55. Spruell, J. M.; Coskun, A.; Friedman, D. C.; Forgan, R. S.; Sarjeant, A. A.; Trabolsi, A.; Fahrenbach, A. C.; Barin, G.; Paxton, W. F.; Dey, S. K.; Olson, M. A.; Benîtez, D.; Tkatchouk, E.; Colvin, M. T.; Carmielli, R.; Caldwell, S. T.; Rosair, G. M.; Hewage, S. G.; Duclairoir, F.; Seymour, J. L.; Slawin, A. M. Z.; Goddard, W. A.; Wasielewski, M. R.; Cooke, G.; Stoddart, J. F., Highly Stable Tetrathiafulvalene Radical Dimers In [3]Catenanes. *Nat. Chem.* **2010,** *2* (10), 870-879.

56. Wudl, F.; Smith, G. M.; Hufnagel, E. J., Bis-1,3-Dithiolium Chloride: An Unusually Stable Organic Radical Cation. *J. Chem. Soc., Chem. Commun.* **1970,** (21), 1453-1454.

57. Ziganshina, A. Y.; Ko, Y. H.; Jeon, W. S.; Kim, K., Stable π-dimer Of A Tetrathiafulvalene Cation Radical Encapsulated In The Cavity Of Cucurbit[8]Uril. *Chem. Commun.* **2004,** (7), 806-807.

58. Bigot, J.; Charleux, B.; Cooke, G.; Delattre, F.; Fournier, D.; Lyskawa, J.; Sambe, L.; Stoffelbach, F.; Woisel, P., Tetrathiafulvalene End-Functionalized Poly(N-isopropylacrylamide): A New Class of Amphiphilic Polymer for the Creation of Multistimuli Responsive Micelles. *J. Am. Chem. Soc.* **2010,** *132* (31), 10796-10801.

59. Sun, W.; Xu, C.-H.; Zhu, Z.; Fang, C.-J.; Yan, C.-H., Chemical-Driven Reconfigurable Arithmetic Functionalities Within a Fluorescent Tetrathiafulvalene Derivative. *J. Phys. Chem. C* **2008,** *112* (43), 16973-16983.

60. Guldi, D. M.; Sànchez, L.; Martín, N., Formation and Characterization of the π-Radical Cation and Dication of π-Extended Tetrathiafulvalene Materials. *J. Phys. Chem. B* **2001,** *105* (29), 7139-7144.

61. Halling, M. D.; Bell, J. D.; Pugmire, R. J.; Grant, D. M.; Miller, J. S., Solid-State NMR Spectra and Long, Intra-Dimer Bonding in the π-$[TTF]_2^{2+}$ (TTF = Tetrathiafulvalene) Dication. *J. Phys. Chem. A* **2010,** *114* (24), 6622-6629.

62. Akutagawa, T.; Kakiuchi, K.; Hasegawa, T.; Noro, S.-I.; Nakamura, T.; Hasegawa, H.; Mashiko, S.; Becher, J., Molecularly Assembled Nanostructures of a Redox-Active Organogelator. *Angew. Chem. Int. Ed.* **2005,** *44* (44), 7283-7287.

63. Giffard, M.; Gorgues, A.; Riou, A.; Roncali, J.; Alonso, P.; Uriel, S.; GarÌn, J.; Nguyen, T. P., Generation Of Radicals And Formation of Conducting Materials By Protic Doping of Tetrahiafulvalenes. *Synt. Met.* **1995,** *70*, 1133-1134.

64. Williams, J. M.; Schultz, A. J.; Geiser, U.; Carlson, K. D.; Kini, A. M.; Wang, H. H.; Kwok, W.-K.; Whangbo, M.-H.; Schirber, J. E., Organic Superconductors-New Benchmarks. *Science* **1991,** *252* (5012), 1501-1508.

65. Kobayashi, Y.; Yoshioka, M.; Saigo, K.; Hashizume, D.; Ogura, T., Hydrogen-Bonding-Assisted Self-Doping in Tetrathiafulvalene (TTF) Conductor. *J. Am. Chem. Soc.* **2009,** *131* (29), 9995-10002.

66. Wenger, S.; Bouit, P. A.; Chen, Q.; Teuscher, J.; Censo, D. D.; Humphry-Baker, R.; Moser, J. E.; Delgado, J. L.; Martín, N.; Zakeeruddin, S. M.; Grätzel, M., *J. Am. Chem. Soc.* **2010,** *132*, 5164.

67. Sun, L.; Campbell, M. G.; Dincă, M., Electrically Conductive Porous Metal–Organic Frameworks. *Angew. Chem. Int. Ed. Engl.* **2016,** *55* (11), 3566-3579.

68. Jana, A.; Bähring, S.; Ishida, M.; Goeb, S.; Canevet, D.; Sallé, M.; Jeppesen, J. O.; Sessler, J. L., Functionalised Tetrathiafulvalene- (TTF-) Macrocycles: Recent Trends In Applied Supramolecular Chemistry. *Chem. Soc. Rev.* **2018,** *47* (15), 5614-5645.

69. Wang, H.-Y.; Cui, L.; Xie, J.-Z.; Leong, C. F.; D'Alessandro, D. M.; Zuo, J.-L., Functional Coordination Polymers Based On Redox-Active Tetrathiafulvalene And Its Derivatives. *Coord. Chem. Rev.* **2017,** *345*, 342-361.

70. Coskun, A.; Spruell, J. M.; Barin, G.; Fahrenbach, A. C.; Forgan, R. S.; Colvin, M. T.; Carmieli, R.; Benítez, D.; Tkatchouk, E.; Friedman, D. C.; Sarjeant, A. A.; Wasielewski, M. R.; Goddard, W. A.; Stoddart, J. F., Mechanically Stabilized Tetrathiafulvalene Radical Dimers. *J. Am. Chem. Soc.* **2011,** *133* (12), 4538-4547.

71. Wang, C.; Dyar, S. M.; Cao, D.; Fahrenbach, A. C.; Horwitz, N.; Colvin, M. T.; Carmieli, R.; Stern, C. L.; Dey, S. K.; Wasielewski, M. R.; Stoddart, J. F., Tetrathiafulvalene Hetero Radical Cation Dimerization in a Redox-Active [2]Catenane. *J. Am. Chem. Soc.* **2012,** *134* (46), 19136-19145.

72. Spanggaard, H.; Prehn, J.; Nielsen, M. B.; Levillain, E.; Allain, M.; Becher, J., Multiple-Bridged Bis-Tetrathiafulvalenes: New Synthetic Protocols and Spectroelectrochemical Investigations. *J. Am. Chem. Soc.* **2000,** *122* (39), 9486-9494.

73. Davis, C. M.; Lim, J. M.; Larsen, K. R.; Kim, D. S.; Sung, Y. M.; Lyons, D. M.; Lynch, V. M.; Nielsen, K. A.; Jeppesen, J. O.; Kim, D.; Park, J. S.; Sessler, J. L., Ion-Regulated Allosteric Binding of Fullerenes (C_{60} and C_{70}) by Tetrathiafulvalene-Calix[4]pyrroles. *J. Am. Chem. Soc.* **2014,** *136* (29), 10410-10417.

74. Bejger, C.; Davis, C. M.; Park, J. S.; M. Lynch, V.; Love, J. B.; Sessler, J. L., Palladium Induced Macrocyclic Preorganization for Stabilization of a Tetrathiafulvalene Mixed-Valence Dimer. *Org. Lett.* **2011,** *13* (18), 4902-4905.

75. Yoshizawa, M.; Kumazawa, K.; Fujita, M., Room-Temperature and Solution-State Observation of the Mixed-Valence Cation Radical Dimer of Tetrathiafulvalene, $[(TTF)_2]+$, within a Self-Assembled Cage. *J. Am. Chem. Soc.* **2005,** *127* (39), 13456-13457.

76. Adeel, S. M.; Li, Q.; Nafady, A.; Zhao, C.; Siriwardana, A. I.; Bond, A. M.; Martin, L. L., A Systematic Study of The Variation of Tetrathiafulvalene (TTF), $TTF^{\bullet+}$ And TTF^{2+} Reaction Pathways With Water In The Presence And Absence of Light. *RSC Adv.* **2014,** *4* (91), 49789-49795.

77. Legros, J.-P.; Bousseau, M.; Valade, L.; Cassoux, P., Crystal Structure of a Non-Conductive Non-Stoichiometric Tetrathiafulvalenium Salt: $(TTF)_3(BF_4)_2$. *Mol. Cryst. Liq. Cryst.* **1983,** *100* (1-2), 181-192.

78. Olaya, A. J.; Hidalgo-Acosta, J. C.; Omatsu, T.; Girault, H. H., Photosensitized Hydrogen Evolution on a Floating Electrocatalyst Coupled to Electrochemical Recycling. *J. Am. Chem. Soc.* **2018,** *140* (32), 10149-10152.

79. Olaya, A. J.; Ge, P.; Gonthier, J. F.; Pechy, P.; Corminboeuf, C.; Girault, H. H., Four-Electron Oxygen Reduction by Tetrathiafulvalene. *J. Am. Chem. Soc.* **2011,** *133* (31), 12115-12123.

80. Rosokha, S. V.; Kochi, J. K., Molecular and Electronic Structures of the Long-Bonded π-Dimers of Tetrathiafulvalene Cation-Radical in Intermolecular Electron Transfer and in (Solid-State) Conductivity. *J. Am. Chem. Soc.* **2007,** *129*, 828.

81. Desiraju, G. R., Supramolecular Synthons in Crystal Engineering—A New Organic Synthesis. *Angew. Chem. Int. Ed. Engl.* **1995,** *34*, 2311–2327.

82. Iyoda, M.; Hasegawa, M., Star-Shaped Tetrathiafulvalene Oligomers Towards The Construction Of Conducting Supramolecular Assembly. *Beilstein J. Org. Chem.* **2015,** *11*, 1596-1613.

83. Favier, F.; Liu, H.; Penner, R. M., Size-Selective Growth of Nanoscale Tetrathiafulvalene Bromide Crystallites on Platinum Particles. *Adv. Mater.* **2001,** *13*, 1567-1570.

84. Scott, B. A.; La Placa, S. J.; Torrance, J. B.; Silverman, B. D.; Welber, B., The Crystal Chemistry Of Organic Metals. Composition, Structure, And Stability In The Tetrathiafulvalinium-Halide Systems. *J. Am. Chem. Soc.* **1977,** *99* (20), 6631-6639.

TOC

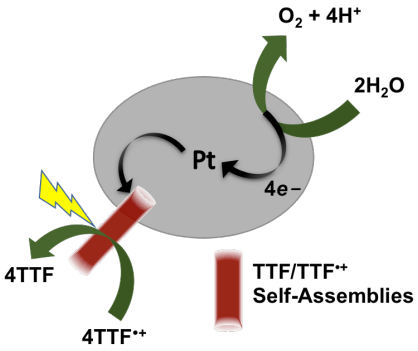
$O_2 + 4H^+$
$2H_2O$
Pt
4e–
4TTF
$4TTF^{\bullet+}$
$TTF/TTF^{\bullet+}$
Self-Assemblies

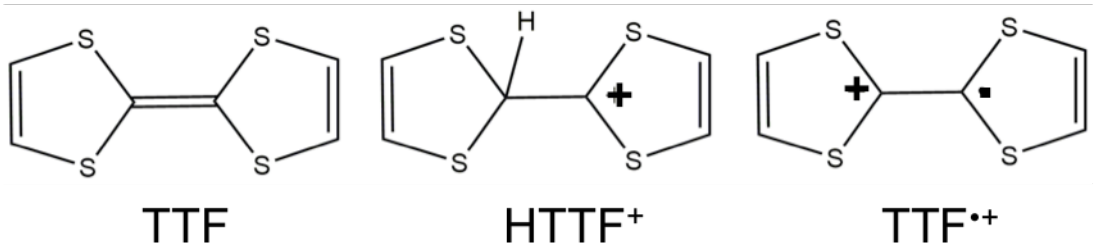
S
S
S
S
TTF
H
S
S
S
S
+
HTTF+
S
S
S
S
+
•
TTF•+

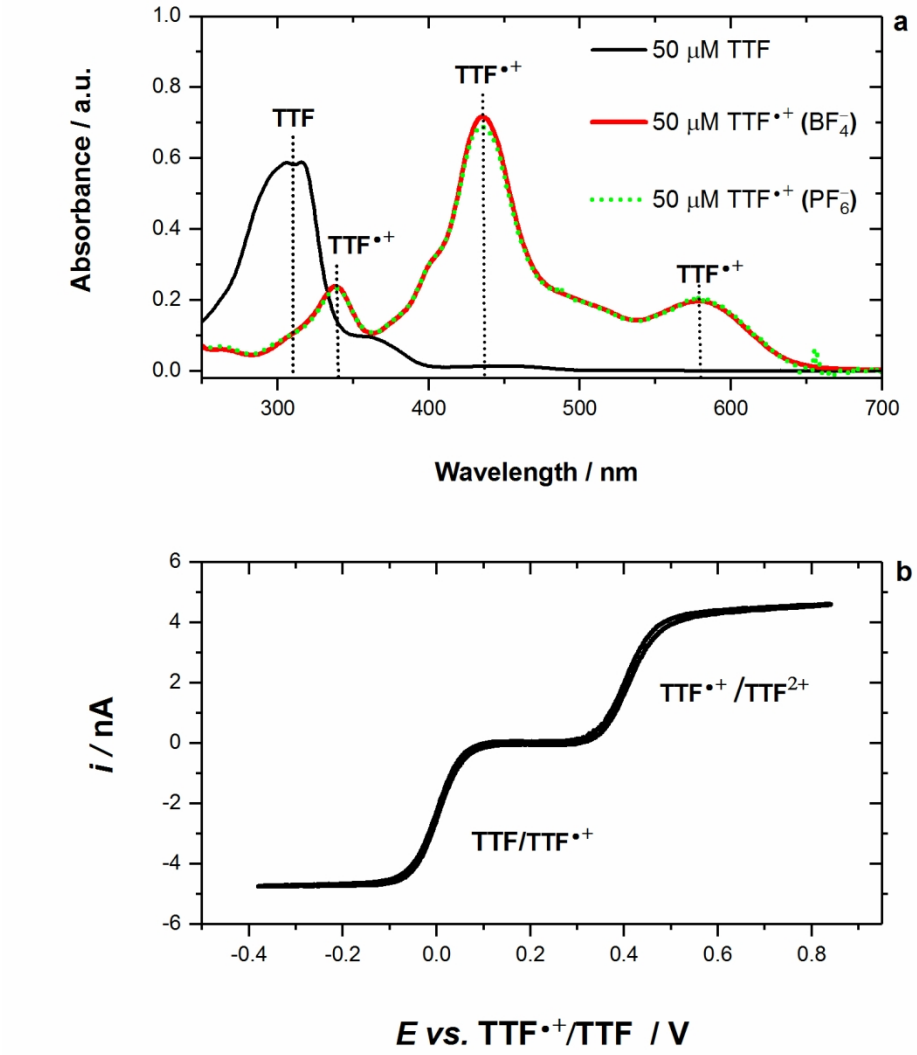

Figure 1. a. UV-vis absorption spectra in dry MeCN of 50 μM TTF and 50 μM $TTF^{\bullet+}$ with BF_4^- and PF_6^- as counter-ions (CI). b. Cyclic voltammogram of 1.0 mM $TTF^{\bullet+}$ (as CI) in dry MeCN (0.1 M $TBAPF_6$ as supporting electrolyte) taken with a 8 μm carbon microelectrode. The scan rate was 25 $mV \cdot s^{-1}$.

143x166mm (300 x 300 DPI)

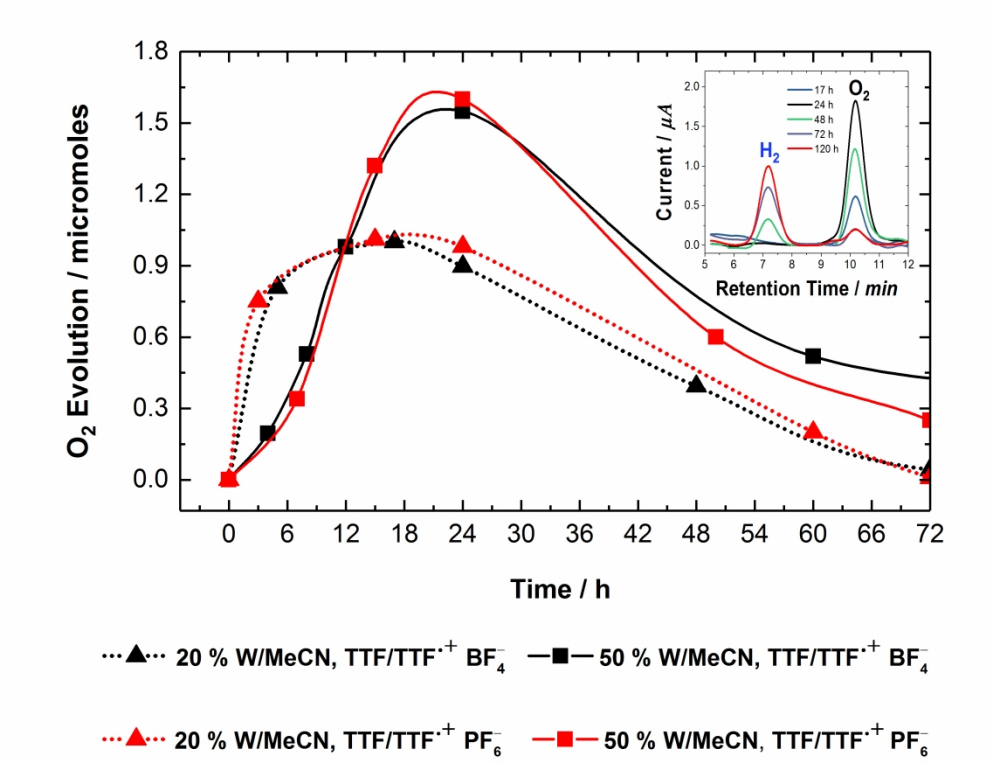

Figure 2. Gas evolution during photosensitized WOR. Initial conditions: 2 mM $TTF^{\bullet+}$ and 1 mg Pt (< 10 μm) in 20% v/v (dotted lines) and 50 % v/v (full lines) water/MeCN (W/MeCN) mixtures. Black and red plots correspond to the photocatalytic experiments performed with $TTF/TTF^{\bullet+}BF_4^-$ and $TTF/TTF^{\bullet+}PF_6^-$, respectively. All the samples were vigorously stirred and irradiated with a 455 nm LED. Inset: chromatograms obtained at different moments of the WOR by $TTF/TTF^{\bullet+}BF_4^-$ in 50 % (v/v) water/MeCN mixtures. Even though the amount of O_2 detected is 50 times higher than that of H_2, the signal associated to H_2 is comparable to that of O_2 due to the detection method. Indeed, the difference in thermal conductivity between H_2 and Ar (carrier gas) is 20 times higher than that between O_2 and Ar, accounting for a higher sensitivity for the detection of H_2.

272x208mm (300 x 300 DPI)

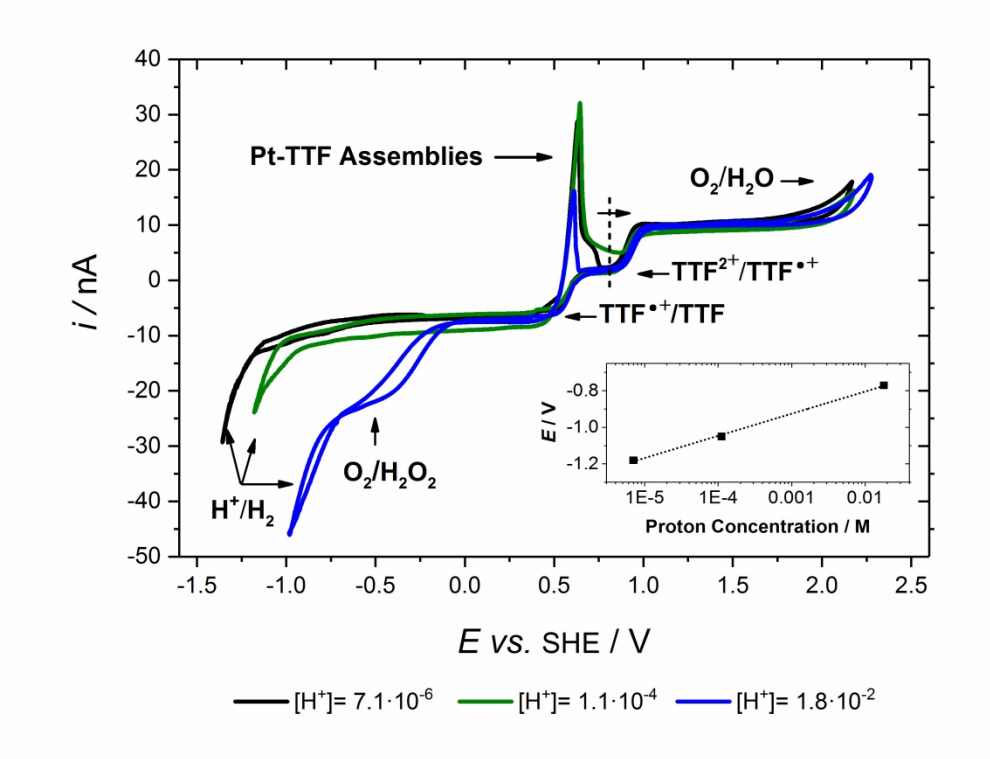

Figure 3. Cyclic voltammograms (CVs) of acidified standards of 1 mM $TTF^{\bullet+}$ (in the form of $TTF/TTF^{\bullet+}BF_4^-$) in 20% Water/MeCN. Concentration of HBF_4: $7.1\cdot10^{-6}$ M, $1.1\cdot10^{-4}$ M and $1.8\cdot10^{-2}$ M. Potential scan: 0.82 V (vertical dashed line) to 2.3 V, followed by 2.3 V to negative potentials and back to 0.75 V. Inset figure: E (onset potential for proton reduction) vs $\log_{10}[H^+]$.

272x208mm (300 x 300 DPI)

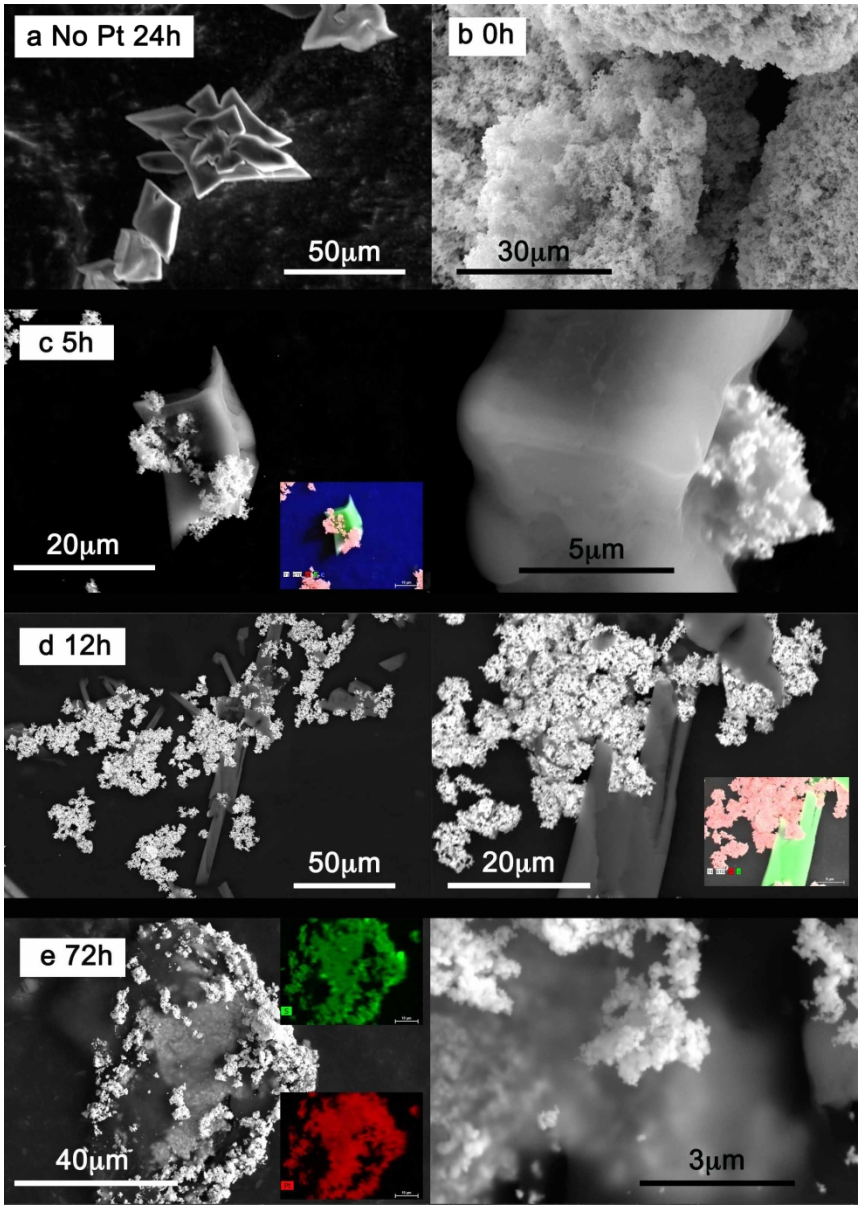

Figure 4. SEM images of TTF-based assemblies during photosensitized WOR. Conditions: $[TTF^{\bullet+}]_0$= 2mM (in the form of $TTF/TTF^{\bullet+}BF_4^-$), Pt=1mg, 50% (v/v) water/MeCN. 30 μL aliquots were dried on carbon paste inside the glove box. The drying time was 1 h for all the samples. The inset figures are EDX images showing the distribution of sulfur (green) and Pt (red). a. $TTF^{\bullet+}$ aged during 24 h in absence of Pt and in dark. WOR progression in time: b. 0h; c. 5h; d. 12h; e. 72h. The images on the right of Figures 4.c, d, and e are close-ups of the corresponding images on the left.

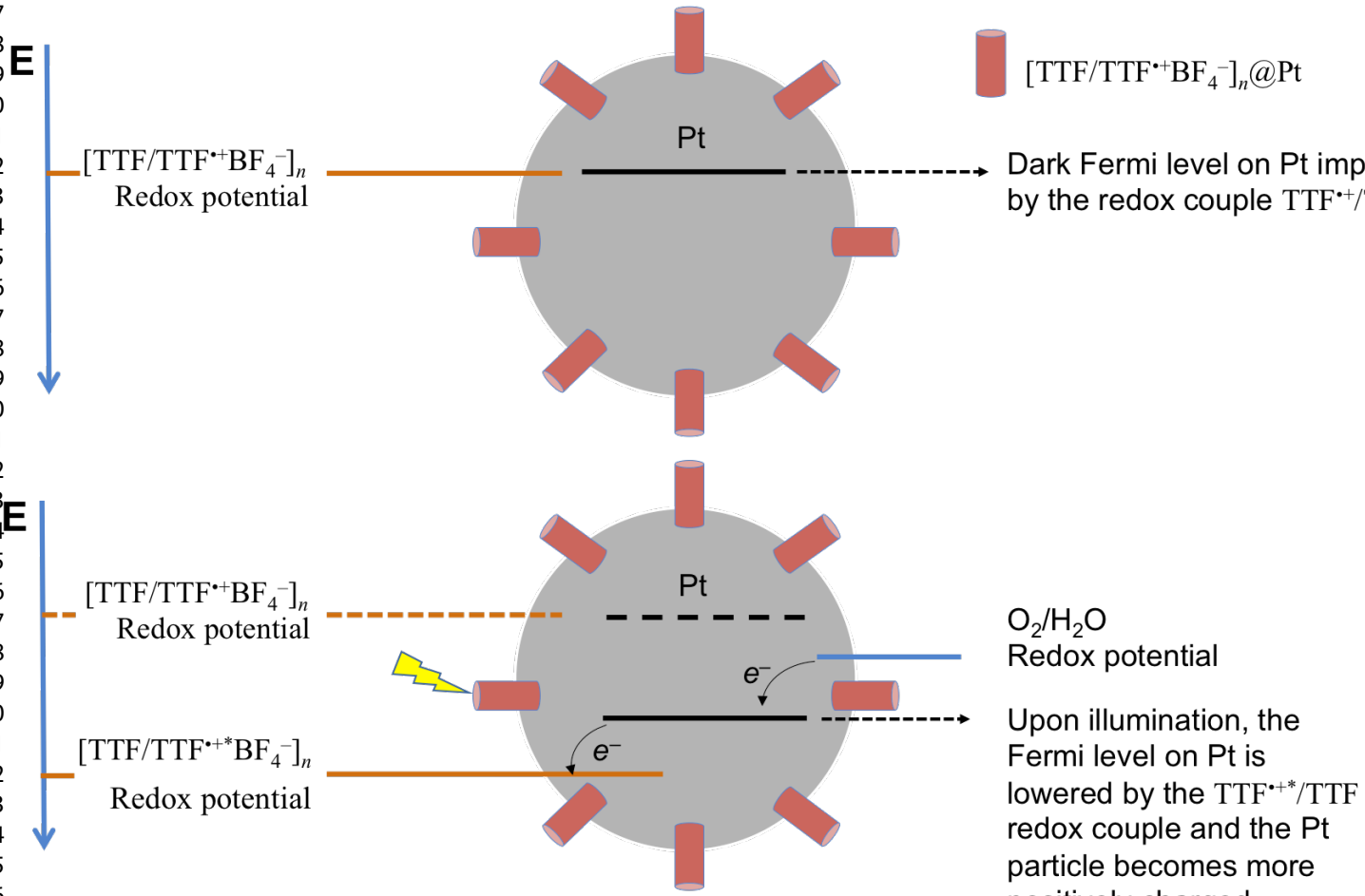
E
[TTF/TTF•+BF4−]n
Redox potential
Pt
[TTF/TTF•+BF4−]n@Pt
Dark Fermi level on Pt imposed by the redox couple TTF•+/TTF
E
[TTF/TTF•+BF4−]n
Redox potential
Pt
O2/H2O
Redox potential
e−
e−
[TTF/TTF•+*BF4−]n
Redox potential
Upon illumination, the Fermi level on Pt is lowered by the TTF•+*/TTF redox couple and the Pt particle becomes more positively charged

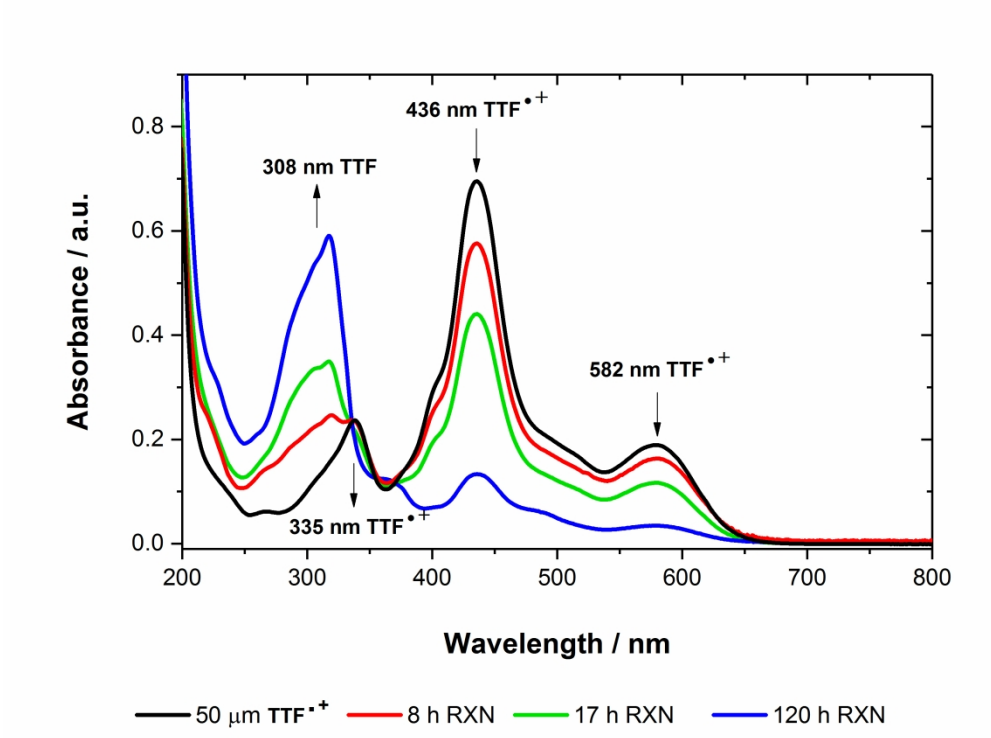

Figure 5. UV-Visible absorption spectra taken during photosensitized WOR by $TTF^{\bullet+}$ (in the form of $TTF/TTF^{\bullet+}BF_4^-$). Initial conditions for the reaction: $[TTF^{\bullet+}]_0$: 2mM, 50% (v/v) water/MeCN, 1 mg of Pt (<10μm), irradiation at 455 nm. All the solutions were diluted down to 50 μM with dry MeCN inside the glove box prior analysis.

272x208mm (300 x 300 DPI)

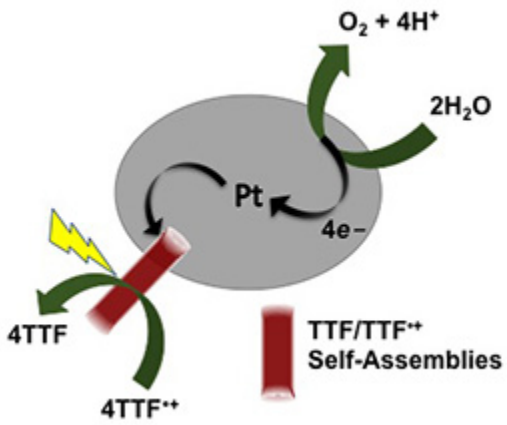
$O_2 + 4H^+$
$2H_2O$
Pt
4e–
4TTF
$4TTF^{\bullet+}$
TTF/$TTF^{\bullet+}$
Self-Assemblies

TOC